PCCP
Physical Chemistry Chemical Physics

This article can be cited before page numbers have been issued, to do this please use: J. Kim, T. Kim, J. Hwang, S. Yoon, S. Lee, C. Kim, J. Park and D. Kim, *Phys. Chem. Chem. Phys.*, 2026, DOI: 10.1039/D6CP01824F.

ROYAL SOCIETY OF CHEMISTRY

rsc.li/pccp

ARTICLE

View Article Online
DOI: 10.1039/D6CP01824F

High-entropy Na layered oxide facilitating reversible oxygen capacity

Received 00th January 20xx,
Accepted 00th January 20xx

DOI: 10.1039/x0xx00000x

Jongbeom Kim , ‡[a] Taesoo Kim, ‡[a] Juncheol Hwang,[a] Sangho Yoon,[a] Seokhyun Lee ,[a]

Chunjoong Kim[b], Jungjin Park[c] and Duho Kim [a,*]

Achieving nonhysteretic and reversible (nHR) oxygen redox in sodium-ion batteries(SIBs) is critical for enhancing their energy density and practical viability. Herein, we present a high-throughput computational framework that integrates machine learning interatomic potentials (MLIPs) with density functional theory (DFT) to design high-entropy layered Na-based cathodes with improved redox reversibility. Using MLIP-based screening of 30,240 configurations derived from $Na[Li_{1/6}Mn_{2/6}A_{1/6}B_{1/6}C_{1/6}]O_2$ (A, B, C: 3d transition metals), $Na[Li_{1/6}Mn_{2/6}Ti_{1/6}V_{1/6}Zn_{1/6}]O_2$ (HE-NLMO) is identified as the most thermodynamically stable composition. With understanding of thermodyanmic phase stabilities, DFT calculations reveal that HE-NLMO enables spontaneous and structurally continuous Li-ion migration into tetrahedral sites within the Na layer during desodiation. Electronic structure investigations further show that the selective oxidation behaviours trigger the asymmetric Li position in the Na layer for easily returning it to the original site. This combination of structural and electronic flexibility facilitates a smooth Li-ion migration pathway and sustainable nHR oxygen redox. Our results underscore the effectiveness of entropy engineering and ML-DFT hybrid approaches in accelerating the discovery of high-performance Na-based cathodes.

1. Introduction

To promote the adoption of sustainable energy sources and mitigate the environmental impact of fossil fuel consumption, the development of efficient energy storage systems is indispensable. In light of this, lithium-ion batteries (LIBs) have been extensively studied and deployed as high-capacity electrochemical energy storage devices.[1-6] However, their commercial viability is increasingly challenged by the fluctuating cost and limited natural abundance of lithium.[7, 8] Consequently, considerable research efforts have been directed toward sodium-based alternatives, which substitute lithium with the more abundant sodium to enable cost-effective and sustainable energy storage.[9-13] Despite these advantages, sodium-ion batteries (SIBs) exhibit inherently lower energy densities than those of LIBs, primarily due to the lower chemical potential of sodium ion and its larger ionic radius relative to those of lithium ion, which can adversely affect overall electrochemical performance.[14, 15] To address these fundamental limitations, oxygen redox chemistry has been proposed as a promising strategy to achieve additional capacity by involving lattice oxygen in the redox processes during electrochemical cycling. O3-type $Na[Li_{1/3}Mn_{2/3}]O_2$ has emerged as a promising cathode candidates, exhibiting pure oxygen redox behavior at the electrochemical potentials above ~4.0 V vs. Na^+/Na, and delivering a theoretical capacity of 285 mAh g-1 upon desodiation.[16-20] In this oxide, Mn^{4+} remains electrochemically inactive, ensuring that the oxidation process is solely driven by oxygen ions. Unfortunately, $Na[Li_{1/3}Mn_{2/3}]O_2$ suffers from significant irreversibility between the first charge and subsequent discharge processes, manifesting as severe voltage hysteresis and capacity fading.[21-23] Recent studies have revealed that in-plane migration of Mn ions within the transition metal layer gives rise to the formation of oxygen–oxygen dimers, which destabilize the structure and hinder reversibility.[17, 24, 25] In contrast, Li-ion migration into the sodium layer has been shown to stabilize the layered crystal framework, thereby enhancing the reversibility of the oxygen redox reactions.[17, 26, 27] To facilitate the intriguing concept, two principal strategies have been proposed: i) designing compositions with intrinsically stable frameworks, and ii) introducing dopants to control Li-ion migration pathways. Among these, doping has demonstrated particular promise in enabling Li-ion migration into tetrahedral sites, thereby mitigating structural degradation and promoting reversible oxygen redox activity.[28-32] In parallel, the high-entropy strategy has recently emerged as a promising approach for designing structurally robust Na layered oxide cathodes, where configurational entropy suppresses detrimental phase transitions and transition-metal dissolution upon cycling. Experimental studies on P2-type high-entropy Na layered oxides have confirmed the effectiveness of this strategy, with Ti identified as a key structurally stabilizing dopant in this material

---

[a] *Department of Mechanical Engineering (Integrated Engineering Program), Kyung Hee University, 1732 Deogyeong-daero, Giheung-gu, Yongin, Gyeonggi-do 17104, Republic of Korea*
[b] *Department of Materials Science and Engineering, Chungnam National University, 99 Daehak-ro, Yuseong-gu, Daejeon 34134,* Republic of Korea
[c] *Department of KHU-KIST of Converging Science and Technology, Kyung Hee University(KHU), Seoul, 02447,* Republic of Korea
E-mail : duhokim@khu.ac.kr

View Article Online
DOI: 10.1039/D6CP01824F

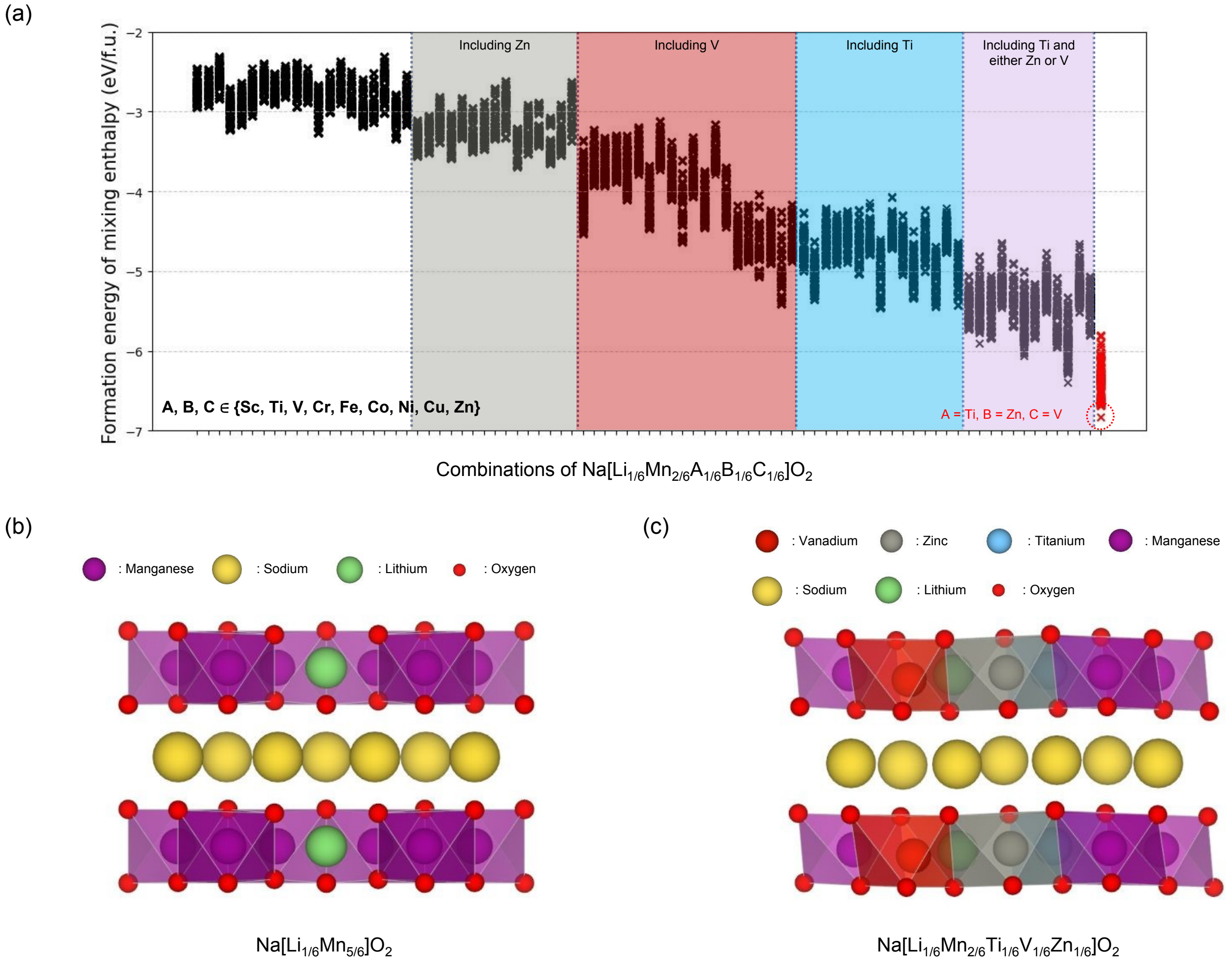

Figure 1. (a) Calculated formation energies of mixing enthalpy for all 30,240 $Na[Li_{1/6}Mn_{2/6}A_{1/6}B_{1/6}C_{1/6}]O_2$ configurations generated by substituting three distinct 3d transition metals {A,B,C ∈ Sc, Ti, V, Fe, Co, Ni, Cu, Zn} at the Li/Mn transition metal sites, followed by full atomic relaxations using MLIPs. Shaded regions highlight configurations containing Zn (gray), V (red), Ti (blue) and Ti together with either Zn or V (purple). The red circle marks the lowest energy configuration. (b) The atomic structures of reference $Na[Li_{1/6}Mn_{5/6}]O_2$ (NLMO). (c) The lowest energy configuration identified from the MLIPs screening: $Na[Li_{1/6}Mn_{2/6}Ti_{1/6}V_{1/6}Zn_{1/6}]O_2$(HE-NLMO).

class.[33, 34] To enable the rational design and systematic exploration of non-hysteretic and reversible (nHR) oxygen redox cathodes, computational approaches based on density functional theory (DFT) have been widely employed to elucidate the redox mechanisms and identify promising candidates. However, the time-consuming nature of DFT calculations poses significant challenges for high-throughput screening, particularly in compositionally complex materials.[35-38] To address this, machine learning interatomic potentials (MLIPs) have been employed to predict atomic structures with DFT-level accuracy at significantly reduced computational cost.[39-45] In this work, we propose a multi-doped Mn layered oxide featuring oxygen redox activity using an integrated computational approach that leverages the complementary strengths of MLIPs and DFT for advanced sodium-ion batteries.[46-48] The former method efficiently generates a large structural dataset of fully intercalated and multi-doped Na-based cathodes, leading to the identification of structurally stable compositions. The latter computation is used to investigate their desodiation behaviors and provide atomistic and electronic insights into reversible redox mechanisms and structural evolution based on thermodynamic phase stabilities. In addition, this hybrid strategies enable rapid screening of high entropy oxygen redox cathodes and offers a robust approach for accelerating the

View Article Online
DOI: 10.1039/D6CP01824F

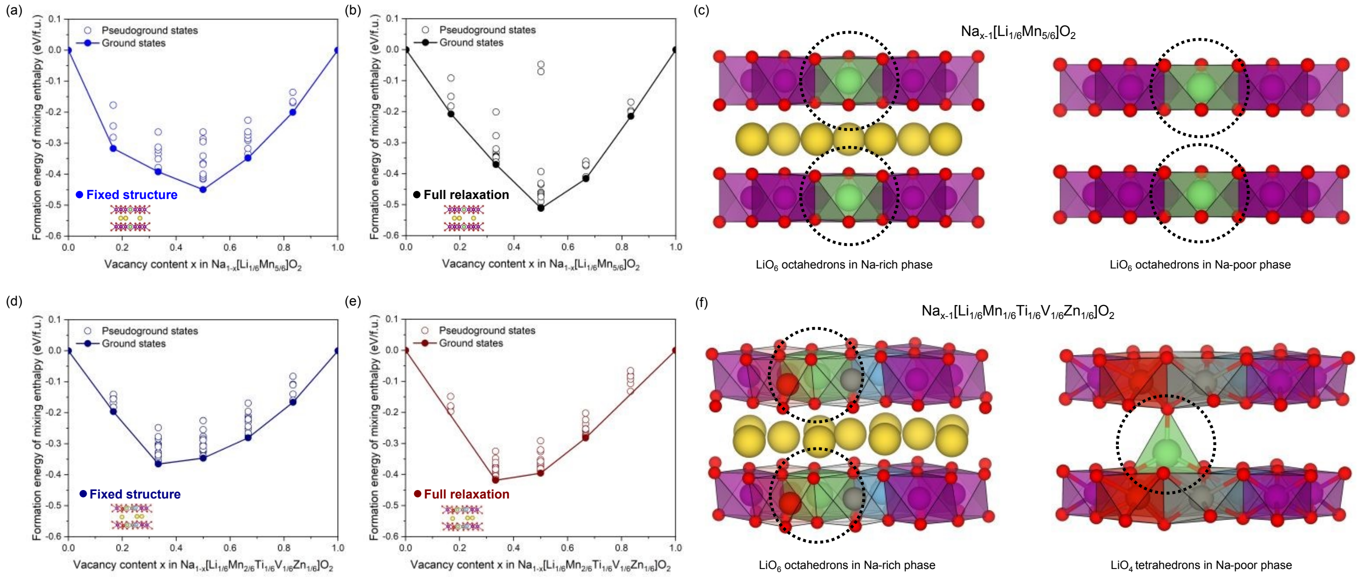

Figure 2. Formation energies of mixing enthalpy as functions of Na vacancy content x in (a, b) $Na_{1-x}[Li_{1/6}Mn_{5/6}]O_2$ and (d, e) $Na_{1-x}[Li_{1/6}Mn_{2/6}Ti_{1/6}V_{1/6}Zn_{1/6}]O_2$over the full range (0.0≤x≤1.0) and their values are calculated based on all possible Na ions and their vacancies. The calculations were carried out depending on the two-type O2- relaxation conditions: (a, d) O^{2-}/O^{n-} (Na/vacancy ordering with fixed structure) and (b, e) O^{2-}/O_2^{2-} (Na/vacancy ordering with full relaxation). The atomic structures under full relaxation condition at x = 0.0 (Na-rich phase) and 1.0 (Na-poor phase) in (c) $Na_{1-x}[Li_{1/6}Mn_{5/6}]O_2$ and (f) $Na_{1-x}[Li_{1/6}Mn_{2/6}Ti_{1/6}V_{1/6}Zn_{1/6}]O_2$

development of next-generation SIBs.

2. Results and discussion

2-1. High-throughput composition screening via MLIPs for Na layered oxides.

To achieve nHR oxygen redox in Na-based cathode materials, two main strategies have been widely explored: i) compositional tuning and ii) elemental doping. Additionally, previous studies have shown that elemental doping can promote Li-ion migration into tetrahedral sites, which contributes to phase stabilization and facilitates a reversible redox process.[20, 28] These considerations led us to integrate both approaches to identify a promising candidate via high-throughput screening, followed by evaluation using DFT calculations. The compositionally tuned $Na[Li_{1/6}Mn_{5/6}]O_2$ (NLMO) was selected as a reference cathode model, considering previous reports indicating the potential for reversible oxygen redox activity. We systematically constructed all possible configurations by substituting 3d transition metals (Sc, Ti, V, Cr, Fe, Co, Ni, Cu, Zn) into the atomistic Mn and Li sites with respect to 2b and 4g Wyckoff positions, respectively.[30, 49-51] The total number of distinct configurations (N) was calculated as:

$$N = \binom{9}{3} \times \binom{5}{2} \times 3! \times \binom{6}{1} = 30{,}240$$

, where the first term corresponds to the selection of three distinct dopant elements from nine candidates, which are 3d transition metals (Sc, Ti, V, Cr, Fe, Co, Ni, Cu, Zn), the second term represents the placement of two Mn atoms among the five remaining transition metal (TM) sites, the third term accounts for the permutations of the three dopants, and the final term indicates the selection of one Li position among the six TM sites. These entire combinations were calculated using MLIPs, followed by full atomic relaxation of each configuration. The MLIP calculations were performed using the pretrained CHGNet v0.3.0 model developed by Deng et al.[42] The original model was pretrained on the Materials Project Trajectory (MPtrj) dataset containing ~1.58 million GGA/GGA+U DFT-calculated structures with corresponding energies, forces, stresses, and magnetic moments. In this work, the pretrained CHGNet model was utilized to perform structural relaxation and energy evaluation for 30,240 $Na[Li_{1/6}Mn_{2/6}A_{1/6}B_{1/6}C_{1/6}]O_2$ configurations. Fig. 1a presents the calculated formation energies of mixing enthalpy for all 30,240 configurations. The gray, red, and blue-colored regions indicate the inclusion of Zn, V, Ti atoms in the configurations respectively, and the purple-colored area represents configurations that simultaneously contain Ti and either Zn or V. The formation energies of mixing enthalpy suggest that doping Zn, V, and Ti enhances the thermodynamic

View Article Online
DOI: 10.1039/D6CP01824F

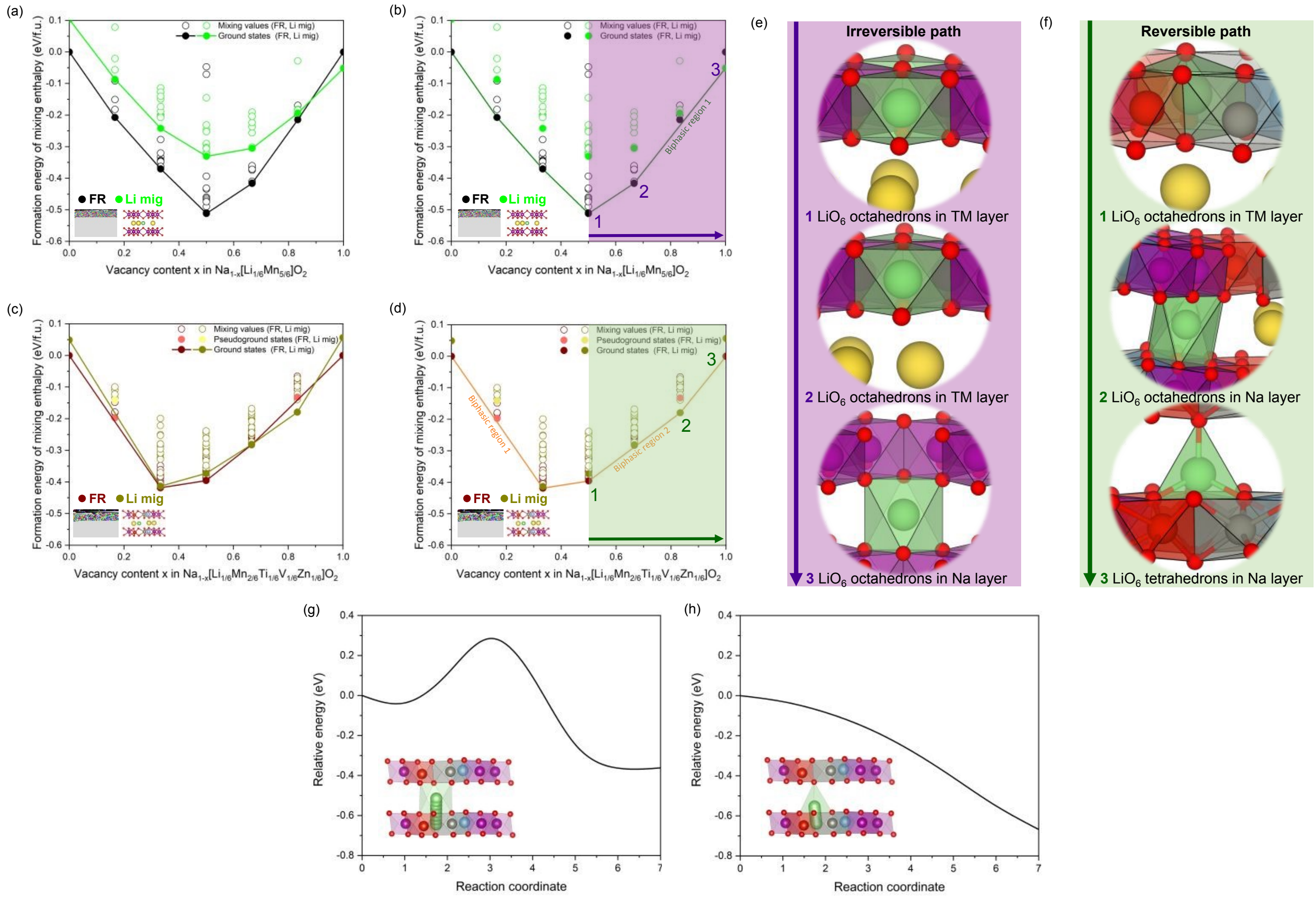

Figure 3. Formation energies of mixing enthalpy as functions of Na vacancy content x in (a) $Na_{1-x}[Li_{1/6}Mn_{5/6}]O_2$ (NLMO) and (c) $Na_{1-x}[Li_{1/6}Mn_{2/6}Ti_{1/6}V_{1/6}Zn_{1/6}]O_2$ (HE-NLMO) over the full range ($0.0 \leq x \leq 1.0$) considering Na/vacancy ordering (black and wine) and Li-ion migration into the Na layer (green and orange). (b) and (d) show the corresponding convex hulls based on the recalculated mixing enthalpies, revealing the presence of monophasic and biphasic regions. The atomic configurations illustrate (e) an irreversible Li-ion migration pathway in NLMO and (f) a reversible pathway in HE-NLMO, corresponding to the regions marked in (b) and (d), respectively. Schematic illustrations of Li-ion migration into octahedral and tetrahedral sites within HE-NLMO at the fully desodiated state, together with the corresponding relative energy profiles for the (g) octahedral and (h) tetrahedral migration pathways, respectively.

stability of the sodium cathode in sequence. The red circle in Fig. 1a denotes the configuration with the lowest formation energy among all $Na[Li_{1/6}Mn_{2/6}A_{1/6}B_{1/6}C_{1/6}]O_2$ compositions including Zn, V, and Ti. The lowest formation energy corresponds to the highest predicted stability, indicating that a high entropy $Na[Li_{1/6}Mn_{2/6}Ti_{1/6}V_{1/6}Zn_{1/6}]O_2$ (HE-NLMO) is the most thermodynamically stable among the evaluated candidates. To cross-validate the MLIP-based screening results, DFT calculations were additionally performed on representative triplet combinations. As shown in Fig. S2, the DFT-calculated formation energies are consistent with the MLIP predictions, confirming that the [Ti, V, Zn] combination yields the lowest mixing enthalpy among the evaluated compositions. The multi-cation substitution in HE-NLMO provides a configurational entropy of mixing (ΔS_{mix}) of $1.56R \approx 12.98$ J mol^{-1} K^{-1}, calculated using the ideal solution model ($\Delta S_{mix} = -R\ \Sigma\ x_i \ln x_i$). This value exceeds the widely accepted $1.5R$ threshold for high-entropy classification, confirming that HE-NLMO is a genuine high-entropy oxide. The total Gibbs free energy of mixing $\Delta G_{mix} = \Delta H_{mix} - T\Delta S_{mix}$, confirming that entropy engineering is an effective strategy for thermodynamically stabilising the single-phase high-entropy layered oxide. Fig. 1b shows the atomic structure of reference NLMO cathode and Fig. 1c displays the atomic structure of HE-NLMO. Based on the high-throughput screening results using MLIPs, HE-NLMO is expected to possess a stable framework promoting the Li-ion migration into tetrahedral sites, which is essential for achieving nHR oxygen redox. In the present framework, the MLIP (CHGNet v0.3.0) was applied exclusively to screen 30,240 candidate compositions at the fully sodiated state ($x = 0$), where it reliably captures relative

View Article Online
DOI: 10.1039/D6CP01824F

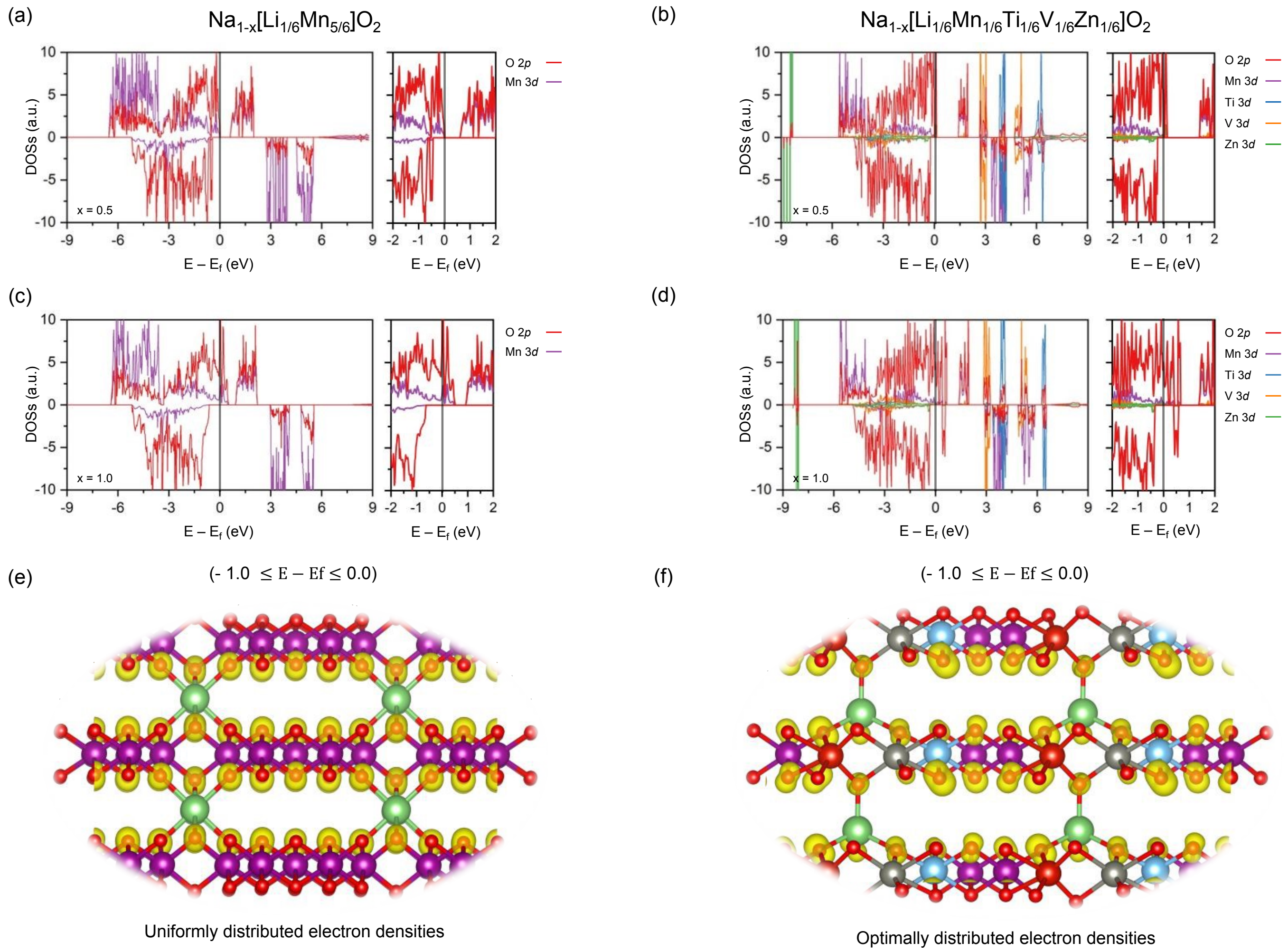

Uniformly distributed electron densities

Optimally distributed electron densities

Figure 4. (a, c) Combined profiles of partial density of states of Mn 3d-electrons and O 2p-electrons at x = 0.5 and 1.0 in Na$_{1-x}$[Li$_{1/6}$Mn$_{5/6}$]O$_2$ (NLMO). (b, d) Combined profiles of partial density of states of Mn, Ti, V, Zn 3d- and O 2p-electrons at x = 0.5 and 1.0 in Na$_{1-x}$[Li$_{1/6}$Mn$_{2/6}$Ti$_{1/6}$V$_{1/6}$Zn$_{1/6}$]O$_2$ (HE-NLMO). The corresponding spatial charge density distributions integrated over the energy range of -1.0 ≤ E-E$_f$≤0.0 in the fully desodiated state for (e) NLMO and (f) HE-NLMO.

structural stabilities among compositionally diverse configurations. All subsequent thermodynamic analyses of the desodiation process (x = 0 to x = 1), including convex hull construction, pseudo-ground state identification, Li-ion migration pathway analysis, and electronic structure calculations, were performed using DFT to ensure accuracy across the full sodiation range.

2-2. Investigation of structural stability and redox reversibility

To evaluate the reversibility of the high-entropy cathode, thermodynamic DFT calculations were conducted for both NLMO and HE-NLMO during the desodiation process. Fig. 2a and b present the formation energies of mixing enthalpy as condition for eliminating structural changes as an idealized desodiation reaction by constructing convex hulls from the lowest-energy values. As the Na/vacancy content increases during the desodiation process, larger discrepancies are observed

View Article Online
DOI: 10.1039/D6CP01824F

between MLIP and DFT calculations, as shown in Fig. S3. Notably, the results for the reference NLMO shown in Fig. 2a and b were reproduced to ensure a consistent comparison with the HE-NLMO.[24] Considering that the thermodynamic energy diagrams provide insights into the thermodynamic phase stability, both NLMO and HE-NLMO oxide models exhibit single-phase behaviors across the entire Na vacancy range, indicating the potential for reversible redox reaction in the ideal condition. The voltage profiles of NLMO and HE-NLMO, derived from the formation energies calculated at various sodiation levels using the average voltage formula, are presented in Fig. S4, providing a direct comparison with experimentally obtainable galvanostatic charge-discharge characteristics. Next, calculations under the fully relaxed (FR) condition were performed to reflect structural changes induced by the desodiation reaction in both cathode models, as shown in Fig. 2b Compared to the monophase reaction upon the overall desodiation for NLMO, the convex-hull diagram for HE-NLMO reveals that there are two biphasic regions of $0.0 \leq x \leq 0.25$ and $0.67 \leq x \leq 1.0$ and it suggests the possibilities of phase separation during the desodiation process.[29] Although the phase separation occurs in the latter range, the pseudo-ground state at x = 0.83 appears very close to the tie line and its phase includes spontaneous Li migration into tetrahedral sites within the Na layer. This result is consistent with the hypothesis that doping facilitates Li migration and improves structural flexibility, thereby enabling reversible intercalation behavior.[29] To further understand the structural responses, the atomic structures of NLMO and HE-NLMO at x = 0.0 and 1.0 are displayed in Fig. 2c and f, respectively. The Li ion located at the octahedral site in the TM layer still remains in the Na-poor phase for NLMO model. In contrast, the Li ion in the fully sodiated structure of HE-NLMO migrates into a tetrahedral site within the Na layer at the Na-poor phase. This behavior suggests that Li migration into the Na layer occurs more readily for HE-NLMO cathode than in NLMO likely due to the structural flexibility introduced by the multi-dopant incorporation. Overall, these findings imply that HE-NLMO model exhibits enhanced reversibility owing to its structural flexibility and the propensity for the Li ion migration into tetrahedral sites during desodiation. Therefore, further calculations explicitly incorporating the Li-migrated structure at the octahedral site within the NaO_6 layer is required to accurately assess the structural stability and redox behavior of HE-NLMO. As presented in Fig. S5, NLMO exhibits an abrupt collapse of lattice parameters at the fully desodiated state (x = 1.0), whereas HE-NLMO shows a continuous and gradual evolution throughout the entire desodiation range, providing quantitative support for the biphasic regions identified under the FR condition.

2-3. Reversible Li-ion migration in high-entropy layered oxides

To investigate the detailed mechanism of Li migration in NLMO and HE-NLMO, we calculated the formation energies of mixing enthalpy under Li migration conditions, as shown in Fig. 3a-d. For better understanding, the calculation mode of Li migration is described in Fig. S1. In particular, the results for NLMO shown in (a) and (b) were reproduced from a previous study to provide a baseline for comparing the phase stability of the HE-NLMO.[24] Based on relative phase stability depending on the Li positions, we combined the formation energies from the two calculation modes, i) FR and ii) Li-migration modes, at the same vacancy content and recalculated the convex hull to examine the phase reaction pathway, as shown in Fig. 3c-d.[29] In the recalculated formation energy, a biphasic reaction emerges for $0.67 \leq x \leq 1.0$ in $Na_{1-x}[Li_{1/6}Mn_{5/6}]O_2$, and its result indicates the onset of phase separation in the deeply desodiated state. Similarly, a biphasic reaction appears above x = 0.5 in $Na_{1-x}[Li_{1/6}Mn_{2/6}Ti_{1/6}V_{1/6}Zn_{1/6}]O_2$. These deeply desodiated states highlighted with purple (NLMO) and green (HE-NLMO) are closely related to evaluating oxygen redox reversibility, thereby enabling identification of the thermodynamic pathway of Li ion in the Na-poor region as a function of the vacancy content (x). Fig. 3e-f show the corresponding atomic configurations at x = 0.5, 0.67, and 1.0 in $Na_{1-x}[Li_{1/6}Mn_{5/6}]O_2$ and x = 0.5, 0.83, and 1.0 in $Na_{1-x}[Li_{1/6}Mn_{2/6}Ti_{1/6}V_{1/6}Zn_{1/6}]O_2$. Based on the phase stabilities inferred from the formation energy landscapes, the Li ion thermodynamics notably differ between the two cathode models. For the NLMO model, the Li ion remains in the TM layer until x = 0.67 but abruptly migrates to an octahedral site in the Na layer at the fully desodiated state. The sudden interlayer migration of Li ion under the phase separation implies structural instability leading to the irreversibility of the redox process. In contrast, for HE-NLMO model, the Li ion in the TM layer at x = 0.5 first migrates to an octahedral site in the Na layer and then spontaneously transitions to a nearby tetrahedral site. Additionally, the nudged elastic band (NEB) calculations shown in Fig. 3g-h provide direct kinetic evidence for this migration pathway. The calculated energy profiles reveal that Li-ion migration toward the tetrahedral site proceeds without a significant migration barrier, indicating that the tetrahedral configuration is energetically favorable in the deeply desodiated state. This gradual and reversible migration pathway indicates enhanced structural flexibility and a higher likelihood of sustaining reversible redox activity. This behavior is attributed to the presence of multi-dopants, which stabilize the Na-poor phase and enabling the Li ion to move more freely between TM and Na layers. Overall, the distinct differences in Li ion migration between NLMO and HE-NLMO models suggest that the multi-dopant-induced structural flexibility is a major factor in facilitating more gradual and reversible Li-ion movement. Additionally, Na-ion transport behavior was further examined using SevenNet-Omni machine-learning potential molecular dynamics (MLP-MD) simulations. Na-ion diffusion coefficients were estimated from the mean square displacement (MSD) analysis at elevated temperatures and subsequently analyzed using the Arrhenius relationship. The corresponding MSD profiles and Arrhenius fitting results are provided in Figures S6

View Article Online
DOI: 10.1039/D6CP01824F

and S7 of the Supporting Information.[52] In light of these findings, it may play a critical role in stabilizing the Na-poor phase and enhancing overall electrochemical reversibility, which is further examined fundamentally in the next section through electronic structure analysis.

2-4. Selective electron distribution of oxygen ion

To deeply understand the redox behaviors in the Na-poor states, we investigated the electronic structures of the TM and oxygen ions by calculating projected partial density of states (PDOSs) at x = 0.5 and 1.0 in $Na_{1-x}[Li_{1/6}Mn_{5/6}]O_2$ and $Na_{1-x}[Li_{1/6}Mn_{2/6}Ti_{1/6}V_{1/6}Zn_{1/6}]O_2$ cathode models, as shown in Fig. 4a-d. In NLMO, the PDOS profiles reveal that the Mn 3d electrons unhybridize with O 2p electrons in high-energy states below the Fermi level at both x = 0.5 and 1.0. Given this, the electronic structure of Mn ion can be understood to be a fully oxidized state of Mn^{4+} for the reference model. Therefore, further desodiation triggers oxygen oxidation, as evidenced by the oxidized O 2p states appearing above the Fermi level.[29] This oxidation behavior occurs concurrently with Li migration into the Na layer, which leads to vacancy formation in the TM layer. Additionally, it may trigger inter- and intra-layer Mn ion migration and facilitate the formation of undesired O−O bonds. Such structural rearrangements are recognized as critical factors increasing the likelihood of irreversible oxygen redox and practical capacity loss. Similarly, the PDOS graphs for HE-NLMO model show O 2p electrons unhybridized with the multiple TM ions at both x = 0.5 and 1.0. Specifically, the charge imbalance induced by further desodiation is compensated by the oxidation of O 2p electrons in high-energy states below the Fermi level at x = 0.5. This is clearly evidenced by the strong O 2p electronic population for $0.0 \leq E-E_f \leq 1.0$ at x = 1.0 in $Na_{1-x}[Li_{1/6}Mn_{2/6}Ti_{1/6}V_{1/6}Zn_{1/6}]O_2$. To further understand the qualitative oxygen activities and the spatial behavior of redox-active sites, we examined the valence-band spatial charge densities integrated over the energy range of $-1.0 \leq E-E_f \leq 0.0$, as shown in Fig. 4e-f. In NLMO, the electronic density of oxygen is relatively delocalized across the crystal framework, implying that oxidation activity is independent of specific lattice sites. In this context, this spatial distribution may induce a symmetric position for migrated Li ions between TM layers. In contrast, the HE-NLMO results show a selective distribution of electronic densities confined around Mn and Ti ions, compared to those around V and Zn ions. From an electronegativity standpoint, the relatively weaker V−O and Zn−O bonds are more favorable for oxidizing their O 2p electrons upon desodiation than Mn−O and Ti−O bonds. This spatially selective distribution may lead to the asymmetric positioning of migrated Li ions, playing a supportive role in their return to the TM layer. Collectively, these theoretical insights suggest that multi-cation substitution not only stabilizes the electronic structure selectively during desodiation but also enhances Li kinetic flexibility across the interlayer, thereby facilitating reversible oxygen redox.

3. Conclusion

Using an integrated high-throughput framework combining MLIP-based screening with DFT investigations, the high-entropy Mn layered cathode was designed to enhance oxygen redox reversibility upon charging and discharging. Among 30,240 possible configurations, Ti, V, and Zn ions were identified as the most promising candidates incorporated into $Na[Li_{1/6}Mn_{2/6}A_{1/6}B_{1/6}C_{1/6}]O_2$ compositions. DFT computational results confirmed that the HE-NLMO model supports spontaneous and structurally continuous Li migration into the tetrahedral sites within the Na layer, leading to structural stabilization and mitigation of the irreversible Mn ion migration. Electronic structure analyses further demonstrated that the selective oxidation behaviours induce the asymmetric Li position in the Na layer for easily returning it to the original site. These synergistic effects collectively facilitate Li ion movement and enhance the reversibility of the oxygen redox process. Our findings provide a systematic design strategy for developing next-generation high-energy-density SIBs through entropy engineering and mechanistic understanding of reversibility.

4. Methodology

4-1. First-Principles Calculations

Using First-principles calculations were performed using the Vienna Ab initio Simulation Package (VASP) based on density functional theory (DFT) using the projector augmented wave (PAW) method. The generalized gradient approximation (GGA) with the Perdew–Burke–Ernzerhof (PBE) functional was employed to describe exchange-correlation interactions under spin-polarized conditions, together with Gaussian smearing. To properly account for the strong on-site Coulomb interactions of transition-metal 3d electrons, the DFT+U approach was applied to both NLMO and HE-NLMO systems. The U values were specifically assigned as follows: 5.0 eV for Mn, 4.0 eV for V, 4.2 eV for Ti, and 10.0 eV for Zn, consistent with previous studies and ensuring a uniform treatment of the multi-doped transition-metal environments. PAW pseudopotentials were used for all elements; Li and Na were described by two 1s and one 2s electrons, and one 2s and six 3p electrons, respectively. Brillouin-zone sampling was carried out using a Monkhorst-Pack k-point mesh of 4 x 4 x 4 and a plane-wave cutoff energy of 530 eV was adopted for all calculations. All simulations were conducted using a supercell containing six formula units of $Na[Li_{1/6}Mn_{5/6}]O_2$ and $Na[Li_{1/6}Mn_{2/6}Ti_{1/6}V_{1/6}Zn_{1/6}]O_2$. For the reference NLMO model, the supercell consisted of 6 Na, 1 Li, 5 Mn, and 12 O atoms. In the HE-NLMO model, Ti, V, and Zn atoms substituted Mn sites according to the MLIP-based high-throughput screening results. To model the desodiation process, Na_{1-x}[cathode] structures were generated by systematically varying the Na-vacancy concentration over the full range ($0 \leq x \leq 1$), considering all possible Na/vacancy configurations within the alkali-metal layer. Both fixed-structure (FS) and fully relaxed (FR) conditions were employed to distinguish idealized desodiation behavior from structural responses induced by Na extraction. In addition, octahedral and tetrahedral Li-ion migration pathways within the unit cell were explicitly considered to capture Li redistribution during desodiation. All structures were fully relaxed with respect to both atomic positions and lattice parameters until the total energy converged to within 10^{-5} eV and the residual forces on each atom were less than 0.01 eV Å^{-1}. The thermodynamic stability of each configuration was evaluated by calculating the formation energies of mixing enthalpy (H_{mix}) relative to the fully sodiated and fully desodiated states. Here, E denotes the total energy of the system at a given Na-vacancy concentration x.

$$\mathrm{H_{mix}} = \mathrm{E_{Na_{1-x}}[M]O_2} - (1-\mathrm{x})\mathrm{E_{Na}[M]O_2} - \mathrm{xE_{Na}[M]O_2}$$

To investigate the Li-ion migration pathways and the associated energy barriers in HE-NLMO, nudged elastic band (NEB) calculations were performed using six intermediate images generated by linear interpolation along the migration pathways. The calculations were conducted for Li-ion migration toward octahedral and tetrahedral sites within the Na layer at the fully desodiated state. During the NEB calculations, selective dynamics were applied such that only the migrating Li ion was allowed to move, while all other atoms were fixed to preserve the local structural environment.

4-2. MLIP Calculations

To investigate the interfacial properties of Li-ion batteries, we employed a Crystal Hamiltonian Graph neural Network (CHGNet, https://github.com/CederGroupHub/chgnet). All simulations were implemented using the Python materials genomics (Pymatgen, https://pymatgen.org) and the atomic simulation environment (ASE, https://gitlab.com/ase/ase) packages.

CHGNet (version 0.3.0), developed by the Ceder group, utilizes a GNN architecture to predict material properties. Structural optimization was performed using the StructOptimizer function with a convergence criterion of 0.02 eV for ionic force and structural perturbation of 0.1 Å. The FIRE algorithm was adopted to ensure robust and efficient structural relaxation.[53]

Pre-trained models provide in the official CHGNet library (as of December 2023) were used for all MLIP-based screening. The initial structures for all calculations were identical,

including the ab initio simulations; however, the MLIP results differ owing to updates.

Author contributions

J.K. and T.K. contributed equally to this work. The manuscript was written through the contributions of all authors. All authors have given approval to the final version of the manuscript.

Conflicts of interest

There are no conflicts to declare.

Data availability

View Article Online
DOI: 10.1039/D6CP01824F

The data of the above mentioned manuscript are available in the ESI.

Acknowledgements

This research is (partially) funded by the BK21 FOUR program of National Research Foundation of Korea.

Notes and references

1. W. Lee, J. Kim, S. Yun, W. Choi, H. Kim and W.-S. Yoon, *Energy & Environmental Science*, 2020, **13**, 4406–4449.
2. X. Cao, Y. Qiao, M. Jia, P. He and H. Zhou, *Advanced Energy Materials*, 2022, **12**, 2003972.
3. C. M. Costa, J. C. Barbosa, R. Gonçalves, H. Castro, F. Del Campo and S. Lanceros-Méndez, *Energy Storage Materials*, 2021, **37**, 433–465.
4. P. K. Nayak, L. Yang, W. Brehm and P. Adelhelm, *Angewandte Chemie International Edition*, 2018, **57**, 102–120.
5. N. Nitta, F. Wu, J. T. Lee and G. Yushin, *Materials today*, 2015, **18**, 252–264.
6. P. Rozier and J. M. Tarascon, *Journal of The Electrochemical Society*, 2015, **162**, A2490.
7. Y. Sun, N. Liu and Y. Cui, *Nature Energy*, 2016, **1**, 1–12.
8. B. Scrosati and J. Garche, *Journal of power sources*, 2010, **195**, 2419–2430.
9. S. W. Kim, D. H. Seo, X. Ma, G. Ceder and K. Kang, *Advanced Energy Materials*, 2012, **2**, 710–721.
10. S. Y. Hong, Y. Kim, Y. Park, A. Choi, N.-S. Choi and K. T. Lee, *Energy & Environmental Science*, 2013, **6**, 2067–2081.
11. H. Pan, Y.-S. Hu and L. Chen, *Energy & Environmental Science*, 2013, **6**, 2338–2360.
12. N. Yabuuchi, K. Kubota, M. Dahbi and S. Komaba, *Chemical reviews*, 2014, **114**, 11636–11682.
13. H. Kim, H. Kim, Z. Ding, M. H. Lee, K. Lim, G. Yoon and K. Kang, *Advanced Energy Materials*, 2016, **6**, 1600943.
14. R. Usiskin, Y. Lu, J. Popovic, M. Law, P. Balaya, Y.-S. Hu and J. Maier, *Nature Reviews Materials*, 2021, **6**, 1020–1035.
15. Y. Li, Q. Zhou, S. Weng, F. Ding, X. Qi, J. Lu, Y. Li, X. Zhang, X. Rong and Y. Lu, *Nature Energy*, 2022, **7**, 511–519.
16. J. Lee and D. Kim, *Energy & Environmental Science*, 2022, **15**, 4554–4560.
17. Q. Wang, S. Mariyappan, G. Rousse, A. V. Morozov, B. Porcheron, R. Dedryvère, J. Wu, W. Yang, L. Zhang and M. Chakir, *Nature Materials*, 2021, **20**, 353–361.
18. Y. Denis, K. Yanagida, Y. Kato and H. Nakamura, *Journal of the electrochemical society*, 2009, **156**, A417.
19. J. R. Croy, J. S. Park, F. Dogan, C. S. Johnson, B. Key and M. Balasubramanian, *Chemistry of Materials*, 2014, **26**, 7091–7098.
20. J. Kim, S. Yoon, T. Kim, G. Choi, D. Kwon, J. Kee, J. Hwang, W. Min, S. Lee and S. Shin, *Advanced Energy Materials*, 2024, **14**, 2303478.
21. S. L. Cui, M. Y. Gao, G. R. Li and X. P. Gao, *Advanced Energy Materials*, 2022, **12**, 2003885.

22. N. Guerrini, L. Jin, J. G. Lozano, K. Luo, A. Sobkowiak, K. Tsuruta, F. Massel, L.-C. Duda, M. R. Roberts and P. G. Bruce, *Chemistry of Materials*, 2020, **32**, 3733–3740.
23. Y. Zuo, B. Li, N. Jiang, W. Chu, H. Zhang, R. Zou and D. Xia, *Advanced materials*, 2018, **30**, 1707255.
24. S. Park, J. Lee, H. Kim, G. Chioi, S. Koo, J. Lee, M. Cho and D. Kim, *ACS applied materials & interfaces*, 2022, **14**, 19515–19523.
25. J. Lee, S. Park, G. Choi, D. Kwon, J. Kim, H. Kim, M. Cho and D. Kim, *Advanced Energy Materials*, 2022, **12**, 2201319.
26. S. Koo, I. H. Ko, J. Lee, S. M. Kang, S. H. Yu and D. Kim, *ChemElectroChem*, 2021, **8**, 1464–1472.
27. R. Clément, J. Xu, D. Middlemiss, J. Alvarado, C. Ma, Y. Meng and C. Greya.
28. J. Lee, J. Kim, S. Park and D. Kim, *Energy Storage Materials*, 2023, **54**, 330–338.
29. S. Park, G. Choi, J. Kim, J. Lee, H. Kim, M. Cho and D. Kim, *Chemistry of Materials*, 2022, **34**, 5971–5979.
30. F. Kong, R. C. Longo, M.-S. Park, J. Yoon, D.-H. Yeon, J.-H. Park, W.-H. Wang, S. Kc, S.-G. Doo and K. Cho, *Journal of Materials Chemistry A*, 2015, **3**, 8489–8500.
31. P. Suresh, A. Shukla and N. Munichandraiah, *Journal of power sources*, 2006, **161**, 1307–1313.
32. X. M. Wu, R. X. Li, S. Chen, Z. Q. He and M. F. Xu, *Bulletin of Materials Science*, 2008, **31**, 109–113.
33. A. Massaro, S. Porporato, M. Botros, A. Piovano, H. Darjazi, D. Stenzel, G. Meligrana, A. B. Muñoz-García, B. Breitung and M. Pavone, *Journal of Materials Chemistry A*, 2026.
34. J. Wang, S. L. Dreyer, K. Wang, Z. Ding, T. Diemant, G. Karkera, Y. Ma, A. Sarkar, B. Zhou and M. V. Gorbunov, *Materials futures*, 2022, **1**, 035104.
35. Z. Wang, X. Feng, Y. Bai, H. Yang, R. Dong, X. Wang, H. Xu, Q. Wang, H. Li and H. Gao, *Advanced Energy Materials*, 2021, **11**.
36. A. Chandrasekaran, D. Kamal, R. Batra, C. Kim, L. Chen and R. Ramprasad, *npj Computational Materials*, 2019, **5**, 22.
37. S. Mohr, M. Eixarch, M. Amsler, M. J. Mantsinen and L. Genovese, *Nuclear Materials and Energy*, 2018, **15**, 64–70.
38. K. Ito, K. Tamura, K. Shimizu, N. L. Yamada, K. Watanabe, K. Suzuki, R. Kanno and M. Hirayama, *RSC Applied Interfaces*, 2024, **1**, 790–799.
39. L. Zhang, H. Wang, R. Car and W. E, *Physical review letters*, 2021, **126**, 236001.
40. C. Chen, W. Ye, Y. Zuo, C. Zheng and S. P. Ong, *Chemistry of Materials*, 2019, **31**, 3564–3572.
41. C. Chen and S. P. Ong, *Nature Computational Science*, 2022, **2**, 718–728.
42. B. Deng, P. Zhong, K. Jun, J. Riebesell, K. Han, C. J. Bartel and G. Ceder, *Nature Machine Intelligence*, 2023, **5**, 1031–1041.
43. A. Merchant, S. Batzner, S. S. Schoenholz, M. Aykol, G. Cheon and E. D. Cubuk, *Nature*, 2023, **624**, 80–85.
44. Z. Cui, Y. Fang, L. Mei, B. Zhang, B. Yu, J. Liu, C. Jiang, Y. Sun, L. Ma and J. Huang, *Nature communications*, 2022, **13**, 2096.
45. S. Kirklin, J. E. Saal, B. Meredig, A. Thompson, J. W. Doak, M. Aykol, S. Rühl and C. Wolverton, *npj Computational Materials*, 2015, **1**, 1–15.
46. D. Kwon and D. Kim, *Journal of Materials Chemistry A*, 2024, **12**, 23837–23847.
47. B. Mortazavi, *Advanced Energy Materials*, 2025, **15**, 2403876.
48. N. Ran, C. Li, Q. Cui, D. Xue and J. Liu, *npj Computational Materials*, 2025, **11**, 208.
49. Z. Moradi, A. Heydarinasab and F. Pajoum Shariati, *International Journal of Quantum Chemistry*, 2021, **121**, e26458.
50. M. Mphahlele, M. Masedi, K. Malatji, P. Ngoepe and R. Ledwaba, 2023.
51. F. Kong, R. C. Longo, D.-H. Yeon, J. Yoon, J.-H. Park, C. Liang, S. KC, S.-K. Doo and K. Cho, *ECS Transactions*, 2015, **64**, 21.
52. J. Kim, J. You, Y. Park, Y. Lim, Y. Kang, J. Kim, H. Jeon, S. Ju, D. Hong and S. Y. Lee, *Nature Communications*, 2026.
53. E. Bitzek, P. Koskinen, F. Gähler, M. Moseler and P. Gumbsch, *Physical review letters*, 2006, **97**, 170201.

View Article Online
DOI: 10.1039/D6CP01824F

Data Availability Statement

The authors confirm that the data supporting the findings of this study are available within the article and its Supplementary materials. Raw data that support the findings of this study are available from the corresponding author, upon reasonable request.